

# Transitional Mixing in a Binary Species Supercritical, Temporal Mixing Layer<sup>1</sup>

Nora Okong'o\* and Josette Bellan\*\*2

Jet Propulsion Laboratory  
California Institute of Technology  
Pasadena, CA 91109-8099

## Abstract

A model of a binary species supercritical temporal mixing layer has been presented and applied to the study of the heptane/nitrogen system. The model contains dynamic conservation equations based on fluctuation-dissipation theory combined with a real gas equation of state and modeled Schmidt and Prandtl numbers so as to correctly portray the relative transport mechanisms. The boundary conditions are periodic in the streamwise and spanwise directions, and non-reflecting outflow in the cross-stream direction based on a real gas analysis derived elsewhere. The initial configuration consists of four vortices and the layer is induced to rollup through the application of an initial perturbation. The four vortices pair up to form an ultimate vortex within which small scales are formed. To determine whether a transitional state has been attained, global temporal characteristics of the layer are examined, as well as vorticity and vorticity magnitude budgets. Furthermore, instantaneous distributions of dynamic and thermodynamic variables are inspected to elucidate the specific features of the layer. This analysis identifies the existence of concentrated high density gradient magnitude regions originating both from the initial density stratification and from the mixing of the two fluids. As regions of increasing magnitude of the density gradient are probed the mixture contains an increasingly large mass fraction of heptane, and the fluid is increasingly non-ideal, meaning that molecular mixing is impeded. The layer also exhibits considerable departures from perfect gas behavior.

## Introduction

The turbulent mixing of fluids at high pressure is a topic of much interest as it is relevant both to natural phenomena and to technical applications. In the realm of technical applications, liquid rocket combustion presents a particular challenge as the operating conditions are supercritical with respect to both fuel and oxidizer, making mandatory the understanding of supercritical fluid behavior for a poten-

tially explosive mixture. In this situation, numerical simulations with validated models can contribute information that would be otherwise impossible to obtain experimentally.

The modeling of supercritical fluid behavior has been primarily addressed in the context of drop modeling. Examples of isolated drop models are those of Umemura and collaborators [33], [34], Curtis and Farrell [5], [6], Jia and Gogos [15], [16], Yang and collaborators [31], [32], [35], Delplanque and Sirignano [8], Daou et al. [7] and Harstad and Bellan [10]. Droplet group effects were modeled by Jiang and Chiang [17], [18], [19] and Harstad and Bellan [11] for monodisperse clusters of drops, and by Harstad and Bellan [13] for polydisperse clusters. Simulations devoted to supercritical shear flows are very scarce (examples being those of Oefelein and Yang [24], [25]) and utilize information obtained from atmospheric pressure turbulence, which introduces uncertainties about their validity. Clearly, a fundamental approach is necessary to unravel the specific aspects of supercritical turbulent shear flows. Such specific aspects have been experimentally observed by Chehroudi et al. [1], [2], and by Mayer and Tamura [21], and include the lack of jet atomization under supercritical condition; instead of drop formation, finger-like structures protruding from the jet are observed.

A contemporary fundamental approach used in fluid mechanics is Direct Numerical Simulation (DNS) whereby all scales of a flow are resolved for Reynolds numbers smaller than those in the fully developed turbulence, but nevertheless reaching the transitional mixing regime. The main artifact of the DNS is to employ a viscosity much larger than that of the real species under consideration so as to enable simulations in a physical domain where the flow is still in the continuum regime. Although this means that the DNS results are not quantitatively correct from the viewpoint of the Reynolds number values, the qualitative behavior of the flow is assumed maintained. Miller et al. [22] have conducted a DNS of a supercritical heptane/nitrogen mixing layer using the validated model of Harstad and Bellan [12] and examined the uncertainties associated with the lack of accurate knowledge of the new transport coefficient, the thermal diffusion factor, which may play an important role at high pressures. However, mixing transition was not achieved in the three dimensional simulation of Miller et al. [22] due to the formation of regions of high density gradient magnitude (called HDGM in the following) which acted as material inter-

<sup>1</sup> Copyright © 2001 by the California Institute of Technology, published with permission by American Institute of Aeronautics and Astronautics, Inc. All rights reserved.

<sup>2</sup>\*Caltech Postdoctoral Scholar, Member AIAA; \*\*Senior Research Scientist, AIAA Associate Fellow (corresponding author, josette.bellan@jpl.nasa.gov).

faces and damped the emerging turbulent eddies. In fact, Okong'o and Bellan [26] showed that the dissipation correlated well with these HDGM regions, and that the layer evolution was the result of two competing processes: entrainment producing strong density gradients (a stabilizing effect) and mixing reducing the density gradients (a destabilizing effect).

The present study uses the general model of Miller et al. [22] but with modified boundary conditions, a larger forcing amplitude and at higher Reynolds numbers, thereby achieving mixing transition. The details of the simulation are presented in Okong'o and Bellan [27], and therefore only the crucial aspects of the model and simulations will be described below. The emphasis of the results is in the specific aspects of the transitional state which reveals visual features that are absent for gaseous layers. Finally, we present a summary and conclusions.

### Model description

The model is based on the fluctuation-dissipation theory of Keizer [20] whose primary result is the form of the flux matrix which now contains additional terms with respect to the traditional Fick and Fourier contributions. This formulation is moreover consistent with non-equilibrium thermodynamics, and relates from first principles forces and fluxes. The general conservation equations are:

$$\frac{\partial \rho}{\partial t} + \frac{\partial}{\partial x_j} [\rho u_j] = 0, \quad (1)$$

$$\frac{\partial}{\partial t} (\rho u_i) + \frac{\partial}{\partial x_j} [\rho u_i u_j + p \delta_{ij} - \tau_{ij}] = 0, \quad (2)$$

$$\frac{\partial}{\partial t} (\rho e_t) + \frac{\partial}{\partial x_j} [(\rho e_t + p) u_j - u_i \tau_{ij} + q_{IK,j}] = 0, \quad (3)$$

$$\frac{\partial}{\partial t} (\rho Y_h) + \frac{\partial}{\partial x_j} [\rho Y_h u_j + j_{hj}] = 0, \quad (4)$$

where  $t$  denotes the time,  $x$  is a Cartesian coordinate, subscripts  $i$  and  $j$  refer to the spatial coordinates,  $u_i$  is the velocity,  $\rho$  is the density,  $e_t = e + u_i u_i / 2$  is the total energy (i.e. internal energy,  $e$ , plus kinetic energy),  $p$  is the thermodynamic pressure, and  $Y_h$  is the mass fraction of heptane. Furthermore,  $\tau_{ij}$  is the Newtonian viscous stress tensor

$$\tau_{ij} = \mu \left[ \frac{\partial u_i}{\partial x_j} + \frac{\partial u_j}{\partial x_i} - \frac{2}{3} \frac{\partial u_k}{\partial x_k} \delta_{ij} \right], \quad (5)$$

where  $\delta_{ij}$  is the Kronecker delta function, and  $\mu$  is the mixture viscosity which is, in general, a function of the thermodynamic state variables. For a binary mixture, such as the one considered here, we duplicate the form of the fluxes given in [12] by noting that  $j_\alpha = m_\alpha \mathbf{J}_\alpha$  and having  $\alpha$  and  $\beta$  take the values  $h$  (heptane) and  $n$  (nitrogen)

$$q_{IK,j} = - \left[ \lambda'_{IK} \frac{\partial T}{\partial x_j} + \alpha_{IK} R_u T \left( \frac{m}{m_n m_h} \right) j'_{hj} \right], \quad (6)$$

$$j_{hj} = - \left[ j'_{hj} + \alpha_{BK} Y_n Y_h \frac{\rho D}{T} \frac{\partial T}{\partial x_j} \right], \quad (7)$$

$$j'_{hj} = \rho D \left[ \alpha_D \frac{\partial Y_h}{\partial x_j} + \frac{Y_n Y_h}{R_u T} \left( \frac{m_n m_h}{m} \right) \left( \frac{v_{,h}}{m_h} - \frac{v_{,n}}{m_n} \right) \frac{\partial p}{\partial x_j} \right] \quad (8)$$

where  $\alpha_{BK}$  and  $\alpha_{IK}$  are the thermal diffusion factors corresponding to the Bearman-Kirkwood (subscript  $BK$ ) and the Irwing-Kirkwood (subscript  $IK$ ) forms of the heat flux ([30]), respectively; they are the new transport coefficients that are introduced by the Soret (in the molar fluxes) and the Dufour (in the heat flux) terms of the transport matrix, and are characteristic of the particular species pairs under consideration. Properties of these thermal diffusion factors are that  $\lim_{p \rightarrow 0} \alpha_{IK} \neq \alpha_{KT}$  and  $\lim_{p \rightarrow 0} \alpha_{BK} = \alpha_{KT}$ . According to [12]

$$\alpha_{IK} = \alpha_{BK} + \frac{1}{R_u T} \left( \frac{m_n m_h}{m} \right) \left( \frac{h_{,h}}{m_h} - \frac{h_{,n}}{m_n} \right), \quad (9)$$

and it is thus necessary to specify only one form of the thermal diffusion factors, the two being related by a thermodynamic function. Here the partial molar enthalpy is  $h_{,\alpha} = (\partial h / \partial X_\alpha)_{T,p,X_\beta(\beta \neq \alpha)}$ , where the molar enthalpy is  $h = G - T(\partial G / \partial T)_{p,X}$  with  $G$  being the Gibbs energy, and the mole fraction  $X$  is related to the mass fraction by  $m_\alpha X_\alpha = m Y_\alpha$  where  $m_\alpha$  is the molecular weight of pure species  $\alpha$ , and the mixture molecular weight is  $m = X_n m_n + X_h m_h$ . The binary diffusion coefficient is  $D$ , the mass diffusion factor is  $\alpha_D$ , the thermal conductivity  $\lambda'_{IK}$  is defined in [12] from the transport matrix and  $R_u$  is the universal gas constant. Furthermore, the molar volume  $v$  is related to the mass density by  $v = m/\rho$ , and the partial molar volume is  $v_{,\alpha} = (\partial v / \partial X_\alpha)_{T,p,X_\beta(\beta \neq \alpha)}$ . It can be shown that  $\lambda'_{IK}$  does not correspond to the kinetic theory (subscript  $KT$ ) definition of the thermal conductivity in that  $\lim_{p \rightarrow 0} \lambda'_{IK} \neq \lambda_{KT}$  but it is related to the thermal conductivity,  $\lambda$ , through

$$\lambda'_{IK} = \lambda + X_n X_h \alpha_{IK} \alpha_{BK} R_u \rho D / m, \quad (10)$$

where  $\lim_{p \rightarrow 0} \lambda = \lambda_{KT}$  as discussed in [12]. The mass diffusion factor  $\alpha_D$  is also a thermodynamic function which is calculated from the fugacity coefficients,  $\varphi_\alpha$  (which are related to the Gibbs energy), as follows:

$$\alpha_D = 1 + X_\alpha \frac{\partial \ln(\varphi_\alpha)}{\partial X_\alpha}, \quad (11)$$

Note that  $\alpha_D$  is independent of which species is chosen in the evaluation.

The details of the adopted equation of state are presented in Miller et al. [22] and will not be duplicated herein. It suffices to state that a Peng - Robinson equation of state is utilized with mixing rules proposed by Harstad et al. [9], and that this choice is both computationally efficient and reasonably accurate since the pure species reference states were found to be accurate to better than 1% relative error through comparisons with the accurate state equations of [9] over the range of variables used in this study.

The configuration used is that of a three-dimensional temporal mixing layer of dimensions  $L_1 \times L_2 \times L_3$

(streamwise  $\times$  cross-stream  $\times$  spanwise) shown in Fig. 1, whose lower stream is heptane and upper stream is nitrogen. The boundary conditions employed are periodic in the streamwise and spanwise directions and non-reflecting outflow conditions in the cross-stream direction based on a characteristic wave approach for real gases as described in Okong'o et al. [28]. The initial configuration consists of four vortices and the layer is induced to rollup through the application of an initial perturbation. The employed disturbance, and the characteristics of the domain size are discussed by Okong'o and Bellan [27] and will not be repeated here. An enlarged discussion on this topic can be found in Okong'o and Bellan [29].

Particular care was devoted to represent the transport coefficients in a self-consistent manner, based on contour plots of the Schmidt,  $Sc$ , and Prandtl,  $Pr$ , numbers using accurate transport properties. Accordingly, the following simplified expressions were used to represent the transport coefficients

$$\mu = \mu_R \left( \frac{T}{(T_1 + T_2)/2} \right)^{0.7}; \quad T \text{ in Kelvins,} \quad (12)$$

$$Sc = \frac{\mu}{\rho \alpha_D D} = 1.5 - Y_h, \quad Pr = \frac{\mu C_p / m}{\lambda} = \frac{Sc}{2 \exp(-3Y_h/2)}, \quad (13)$$

where  $\mu_R$  is a reference viscosity and the reference temperatures  $T_1$  and  $T_2$  correspond to the free stream temperatures for mixing layer simulations. These relations give qualitatively correct trends in that  $Sc$  is respectively greater than or less than unity for the proper mass fractions; however, the maximum value is 1.5 rather than 2, as observed in the contour plots. Eqs. 12 - 13 hold in the following range of thermodynamic state space:  $500K \leq T \leq 1100K$ ,  $6kg/m^3 \leq \rho \leq 286kg/m^3$ , and  $0 \leq Y_h \leq 1$ .

The value of the reference viscosity is determined by the specified value of the initial Reynolds number

$$Re_0 = \frac{0.5(\rho_1 + \rho_2)\Delta U_0 \delta_{\omega,0}}{\mu_R} \quad (14)$$

chosen so as to enable the resolution of all relevant dynamic length scales. The freestream density ( $\rho_1$  or  $\rho_2$ ) is calculated for each pure species at its freestream temperature ( $T_1$  or  $T_2$ ) and at the initial uniform pressure ( $p_0$ ). The vorticity thickness is defined as  $\delta_{\omega}(t) = \Delta U_0 / (\partial U / \partial x_2)_{max}$  where  $U$  is the mean (or  $x_1 - x_3$  planar average) flow in the streamwise direction, and  $\Delta U_0 = U_1 - U_2$  is the velocity difference across the layer. Miller et al. [22] explain the choice of the velocities of the two streams, the intent being to keep the vortices stationary in the computational domain. Whereas the success in this endeavor was not complete, it proved that the choice of

$$U_1 = 2M_c a_{s1} \left[ 1 + \left( \frac{a_{s1}}{a_{s2}} \right) \sqrt{\frac{\rho_1 Z_1}{\rho_2 Z_2}} \right]^{-1}, \quad U_2 = -\sqrt{\frac{\rho_1 Z_1}{\rho_2 Z_2}} U_1, \quad (15)$$

for a real fluid was reasonable, where  $M_c$  is a Mach number and  $Z = p/(\rho T R_u / m)$  is the compression factor. The

specification of  $M_c$  therefore determines  $\Delta U_0$ , and thus ultimately  $\delta_{\omega,0} \equiv \delta_{\omega}(0)$ . The mean streamwise velocity is smoothed near the centerline using an error function profile, as are the mean temperature and mass fraction.

The adopted value of the thermal diffusion factor is  $\alpha_{IK} = 0.1$ , determined by Harstad and Bellan [12] first from a model calibration through comparisons with part of the data from the microgravity experiments of Nomura et al. [23], and further validated in the same study by comparison with the remaining part of Nomura et al.'s [23] data.

## Results

The initial conditions for the simulation analyzed here are: freestream temperatures of  $T_2 = 600$  K and  $T_1 = 1000$  K in the lower and upper stream, respectively, initial pressure  $p_0 = 60$  atm ( $(\rho_2/\rho_1)_0 = 12.88$ ),  $M_c = 0.4$  and  $Re_0 = 500$ . The grid measures  $0.2m \times 0.232m \times 0.12m$  (resolution  $240 \times 288 \times 144$ ) to accommodate four wavelengths in the streamwise and spanwise directions, and the evolution of the layer encompasses rollup and two pairings of the initial spanwise vortices. The initial mean velocity profile is such that  $\delta_{\omega,0} = 6.859 \times 10^{-3}$  m [27]. The results first focus on the assessment of whether a transitional state has been reached. To assess the possible attainment of a transitional state, we analyze several aspects of the global temporal evolution of the mixing layer; according to all the criteria based on these global aspects, the layer did achieve transition. To confirm the results of the temporal evolution, we also inspect the vorticity and vorticity magnitude budgets at the transitional state. Further, to explore the peculiarities of the supercritical mixing layer, we scrutinize visualizations of important dynamic and of all thermodynamic variables. Various characteristics of the fluid are documented at the transitional state, in particular departures from mixing ideality and perfect gas behavior. An enlarged, more thorough investigation of a simulation having the same initial conditions with the exception of  $Re_0$  which is there 600, is available in [27].

### Global temporal characteristics

Mixing layers evolve and grow due to the combined effect of entrainment and small scale formation. Although according to Cortesi et al. [4] the definition of layer growth is not unique, Hernan and Jimenez [14] showed that entrainment is the dominant element in layer growth. Here, the layer growth is measured by the momentum thickness

$$\delta_m = \frac{-1}{(\theta_1 - \theta_2)^2} \int_{-L_{2,min}}^{L_{2,max}} (\theta_2 + \langle \rho u_1 \rangle)(\theta_1 + \langle \rho u_1 \rangle) dx_2 \quad (16)$$

with  $\theta_1 = \langle \rho u_1 \rangle_{x_2=L_{2,max}}$  and  $\theta_2 = \langle \rho u_1 \rangle_{x_2=-L_{2,min}}$ , where  $\langle \rangle$  denotes plane averaging,  $L_{2,max} = -L_2/3$  and  $L_{2,min} = 2L_2/3$ . While the growth is primarily a conse-

quence of entrainment, the product thickness defined as

$$\delta_p = \int \int_V \rho Y_p dV \quad (17)$$

in mass units, where  $Y_p = 2 \min(Y_h, Y_n)$ , is a direct consequence of molecular mixing as explained by [4]. Besides growth and molecular mixing, the evolution of small turbulent scales is a crucial aspect determining whether a layer will reach transition [29]. To evaluate the evolution of the small turbulent scales, we examine the global characteristics of the non-dimensional positive spanwise vorticity,  $\langle\langle \omega_3^+ \rangle\rangle (\delta_{\omega,0}/\Delta U_0)$ , and the non-dimensional enstrophy,  $\langle\langle \omega_i \omega_i \rangle\rangle (\delta_{\omega,0}/\Delta U_0)^2$ ; here  $\langle\langle \rangle\rangle$  denotes volume averaging. Due to the particular form of the initial mean velocity profile, the initial spanwise vorticity is all negative; therefore, the formation of positive spanwise vorticity is a first indication of small scale formation. Moreover, since it is generally believed that stretching increases the enstrophy, its variation is a direct measure of this essential mechanism of turbulence production.

All global characteristics are illustrated in Fig. 2 versus the non-dimensional time  $t^* = t\Delta U_0/\delta_{\omega,0}$ . The non-dimensional momentum thickness,  $\delta_m/\delta_{\omega,0}$ , increases and reaches a plateau at  $t^* = 140$ , this plateau being evidence of the forcing influence on the layer. Further increase in  $\delta_m/\delta_{\omega,0}$  is at a reduced rate, consistent with  $\delta_p/\delta_{p,0}$  exhibiting a slower growth following the plateau, showing that mixing is somewhat abated. Production of positive spanwise vorticity initiates immediately past the layer rollup and continues at a considerable rate until the first pairing after which the rate declines until the second pairing ( $t^* = 135$ ). Past the second pairing,  $\langle\langle \omega_3^+ \rangle\rangle (\delta_{\omega,0}/\Delta U_0)$  reaches a culmination point. Concomitantly, the enstrophy displays a substantial increase rate after rollup and a large peak after each pairing. The small valley coincides with the reduced rate of positive spanwise vorticity production. The second peak in  $\langle\langle \omega_i \omega_i \rangle\rangle (\delta_{\omega,0}/\Delta U_0)^2$  coincides with the second pairing indicating that this event produces considerable stretching. After the second pairing, due to stretching there is a considerable increase in small scale production as evidenced by the  $\langle\langle \omega_3^+ \rangle\rangle (\delta_{\omega,0}/\Delta U_0)$  peak. It is the time station of this  $\langle\langle \omega_3^+ \rangle\rangle (\delta_{\omega,0}/\Delta U_0)$  peak, at  $t^* = 155$ , which is here chosen as the one corresponding to the attainment of the transitional state. At this time, the momentum thickness based Reynolds number,  $Re_m = Re_0(\delta_m/\delta_{\omega,0}) = 1250$ . To determine the state of the layer at  $t^* = 155$ , we first examine the vorticity and vorticity magnitude budgets, and then inspect instantaneous contours in the braid and the between-the-braid planes.

### Vorticity budget at transition

Vorticity is one of the essential features of turbulent flows [3], therefore making it important to examine. The vortic-

ity equation for a compressible flow is

$$\frac{D\omega}{Dt} = (\omega \cdot \nabla)\mathbf{u} - (\nabla \cdot \mathbf{u})\omega - \nabla\left(\frac{1}{\rho}\right) \times \nabla p + \nabla \times \left(\frac{1}{\rho} \nabla \cdot \bar{\tau}\right) \quad (18)$$

where  $D/Dt$  is the substantial derivative, and the equivalent equation for the vorticity magnitude squared follows

$$\begin{aligned} \frac{D(\omega^2)}{Dt} = & 2\omega \cdot (\omega \cdot \nabla)\mathbf{u} - 2(\nabla \cdot \mathbf{u})\omega^2 \\ & - 2\omega \cdot \nabla\left(\frac{1}{\rho}\right) \times \nabla p + 2\omega \cdot \nabla \times \left(\frac{1}{\rho} \nabla \cdot \bar{\tau}\right). \end{aligned} \quad (19)$$

The first term in eqs. 18 and 19 represents the stretching and tilting contribution, the second term describes the effect of dilatation, the third term is the baroclinic participation to vorticity production, and the last term portrays the viscous contribution. Similar to the examination of the global layer characteristics, here we also focus on the spanwise vorticity. Depicted in Figs. 3a and 3b are the non-dimensional homogeneous ( $x_1 - x_3$ ) plane average and plane RMS of the spanwise vorticity budget at  $t^* = 155$ . The largest activity is in the stretching and tilting term, dominating both the average of the budget and the RMS. For all practical purposes, all other terms of the budget average are negligible, whereas for the RMS the order of decreasing activity are the viscous effects, the baroclinic term, and the dilatation. The secondary but not negligible action of viscosity indicates that enough small scales have been formed to promote vorticity destruction by viscous dissipation, but this effect is dominated by small scale formation through stretching and tilting. The budget of the vorticity magnitude squared illustrated in Fig. 4 supports this physical picture. The average is dominated by the negative viscous term diminishing the vorticity magnitude through the action of dissipation, whereas the positive stretching and tilting term is second in order of decreasing magnitude. Both baroclinic and dilatation terms appear negligible. The most prominent RMS contribution is from stretching and tilting, with large peaks across the layer, while the viscous effect closely trails behind. The participation of the dilatation and baroclinic terms is marginal. This physical picture is consistent with the attainment of a transitional state where production of small scales occurs through stretching and tilting, and once formed, these small scales proceed to decrease the magnitude of the vorticity through the action of viscous dissipation.

### Instantaneous visualizations of the transitional state

To confirm the physical picture described above, we examine the distributions of the dynamic and thermodynamic variables in specific planes, at  $t^* = 155$ . Following the interest in the spanwise vorticity, shown in Figs. 5a and 5b are the distributions of the non-dimensional spanwise vorticity,  $\omega_3(\delta_{\omega,0}/\Delta U_0)$ , in the braid and in the between-the-braid planes. Clearly, a large amount of positive spanwise

vorticity has been produced, which is distributed throughout the vortex and distorts it.

Qualitative comparisons between HDGM regions found in the previous pre-transitional study of Miller et al. [22] with the optical observations of Chehroudi et al. [1] who experimentally identified 'wisps' of fluid emerging from a supercritical jet injected into a supercritical medium, were encouraging. The question is whether the same regions of concentrated HDGM may be identified at transition, and if so what is the large  $|\nabla\rho|$  region composition and thermodynamic state. To explore these aspects,  $|\nabla\rho|$ ,  $Y_h$ ,  $\alpha_D$  and  $Z$  are displayed in Figs. 6-9 in the braid (6a - 9a) and the between-the-braid planes (6b - 9b). Not only are the regions of concentrated large  $|\nabla\rho|$  values again evident, but they also appear considerably more convoluted than in the study of [22] conducted with  $Re_0 = 400$ , owing to the substantially higher level of small scales present. Movie visualizations show that the HDGM regions originate both from the initial density stratification and from the mixing of the two species. In fact, the heptane mass fraction contours show parcels of heptane fluid that have 'broken off' from the original stream and have been transported towards the upper nitrogen stream. The mixing region thus formed contains non-ideal fluid ( $\alpha_D < 1$ ) as shown in Figs. 8a and 8b, whereas the two regions of unvitiated species behave as ideal mixtures. Moreover, a detailed analysis [27] shows that as one probes deeper into the HDGM regions (i.e. finds regions closer to the maximum value of  $|\nabla\rho|$  in the entire domain),  $\alpha_D$  decreases and  $Y_h$  increases. Therefore, the HDGM regions are mostly composed of the heavier heptane with some nitrogen present as well, but their molecular mixing is hindered by the non-ideality of the mixture. Thus, the highly distorted nature of the HDGM regions is partially due to poor molecular mixing ( $\alpha_D < 1$ ) during pairing, and also due to the effect of the small scales. To complete the thermodynamic description, we note the considerable departures from the perfect gas behavior displayed in Fig. 9. These departures are evident both in the heptane freestream, and in the mixing layer.

Considering the specific thermodynamic characteristics of the supercritical transitional state, it is foreseen that atmospheric flow turbulent models might not be valid for supercritical flows.

### Summary and conclusions

A model of a supercritical shear layer has been utilized with appropriate boundary conditions to study the transition of a supercritical shear layer to a turbulent state. The achievement of turbulence has been ascertained both from global features of the layer, from an examination of the homogeneous plane average vorticity and vorticity magnitude budgets, and from detailed contour plots at the transitional state. The vorticity and vorticity magnitude budgets corroborate the evidence from the global aspects of the layer in that (i) small scale formation due to stretching and tilting activity dominates the vorticity budget (both

average and RMS) with the viscous effects being second in order of importance, and (ii) viscous effects dominate the vorticity magnitude average with the contribution of the stretching and tilting being also important, while the RMS is primarily dominated by the stretching and tilting term with substantial viscous effects. The physical picture that emerges is that of strong production of turbulent scales through the stretching and tilting mechanism; once produced, these small scales remove vorticity from the flow through the action of viscous dissipation. A tight competition between these formation/destruction mechanisms is evident.

Specific optically related features of the layer due both to the initial density stratification and to mixing are the appearance of regions of high density gradient magnitude. These regions are composed of a mixture of heptane and nitrogen, with the heptane mass fraction increasing as the density gradient magnitude is larger. Moreover, it has been shown elsewhere [27] that as regions of higher magnitude of the density gradient are probed, the mixture becomes increasingly non-ideal, meaning that the fluid has difficulty in mixing at the molecular level. This aspect is highly detrimental to combustion and will have to be mitigated. Additional to the departure from mixture ideality, strong departures from the perfect gas behavior have been documented as well.

Finally, these conclusions are based on this and two other realizations [27], [29], and cannot be considered definitive or applicable to other binary species systems. Additional studies are necessary to unravel the numerous aspects of supercritical fluid mixing.

### Acknowledgments

This research was conducted at the Jet Propulsion Laboratory (JPL), California Institute of Technology. Joint sponsorship was provided by the Air Force Office of Scientific Research with Dr. Julian Tishkoff serving as contract monitor and by the Army Research Office with Dr. David Mann as technical contract monitor, through interagency agreements with the National Space and Aeronautics Administration (NASA). Computational resources were provided by the supercomputing facility at JPL. The authors wish to thank Dr. Mark Carpenter of NASA Langley Research Center and Dr. Kenneth Harstad of JPL for helpful discussions.

### References

- [1] Chehroudi, B., Talley, D. and Coy, E., Initial growth rate and visual characteristics of a round jet into a sub- to supercritical environment of relevance to rocket, gas turbine, and diesel engines, AIAA 99-0206, 37th Aerospace Sciences Meeting, Reno, NV, 1999
- [2] Chehroudi, B., Talley, D. and Coy, E., Fractal geometry and growth rate changes of cryogenic jets near the critical point, AIAA 99-2489, 35th AIAA/ASME/SAE/ASEE Joint Propulsion Conference, Los Angeles, CA, 1999

- [3] Chorin, A., *Vorticity and turbulence*, Springer-Verlag, New York, Inc., 1994
- [4] Cortesi, A. B., Smith, B. L., Yadigaroglu, G. and Banerjee, S., Numerical investigation of the entrainment and mixing processes in neutral and stably-stratified mixing layers, *Phys. Fluids*, 11(1), 162-185, 1999
- [5] Curtis, E.W., and Farrell, P. V., Droplet vaporization in a supercritical microgravity environment, *Acta Astronautica*, 17(11/12), 1189-1193, 1988
- [6] Curtis, E.W., and Farrell, P. V., A numerical study of high-pressure droplet vaporization, *Combust. Flame*, 90, 85-102, 1992
- [7] Daou, J., Haldenwang, P. and Nicoli, C., Supercritical burning of liquid oxygen (LOX) droplet with detailed chemistry, *Combust. Flame*, 101, 153-169, 1995
- [8] Delplanque, J-P. and Sirignano, W. A., Numerical study of the transient vaporization of an oxygen droplet at sub- and super-critical conditions, *Int. J. Heat Mass Transfer*, 36(2), 303-314, 1993
- [9] Harstad, K. G., Miller, R. S., and Bellan, J., Efficient high pressure state equations, *A. I. Ch. E.*, 43(6), 1605-1610, 1997
- [10] Harstad, K. and Bellan, J., Isolated fluid oxygen drop behavior in fluid hydrogen at rocket chamber pressures, *Int. J. Heat Mass Transfer*, 41, 3537-3550, 1998
- [11] Harstad, K. and Bellan, J., Interactions of fluid oxygen drops in fluid hydrogen at rocket chamber pressures, *Int. J. Heat Mass Transfer*, 41, 3551-3558, 1998
- [12] Harstad, K. and Bellan, J., An all-pressure fluid drop model applied to a binary mixture: heptane in nitrogen, *Int. J. of Multiphase Flow*, 26(10), 1675-1706, 2000
- [13] Harstad, K. and Bellan, J., The  $d^2$  variation for isolated LOX drops and polydisperse clusters in hydrogen at high temperature and pressures, in press, *Comb. Flame*, 124, 2000
- [14] Hernan, M. A. and Jimenez, J., Computer analysis of a high-speed film of the plane mixing layer *J. Fluid Mech.*, 119, 323-345, 1982
- [15] Jia, H. and Gogos, G., Investigation of liquid droplet evaporation in subcritical and supercritical gaseous environments, *Journal of Thermophysics and Heat Transfer*, 6(4), 738-745, 1992
- [16] Jia, H. and Gogos, G., High pressure droplet vaporization—effects of liquid-phase solubility, *Int. J. Heat Mass Transfer*, 36(18), 4419-4431, 1993
- [17] Jiang, T. L. and Chiang, W-T., Effects of multiple droplet interaction on droplet vaporization in subcritical and supercritical pressure environments, *Comb. Flame*, 97, 17-34, 1994
- [18] Jiang, T. L. and Chiang, W-T., Vaporization of a dense spherical cloud of droplets at subcritical and supercritical conditions, *Combust. Flame*, 97, 355-362, 1994
- [19] Jiang, T. L. and Chiang, W-T., Transient heating and vaporization of a cool dense cloud of droplets in hot supercritical surroundings, *Int. J. Heat Mass Transfer*, 39(5), 1023-1031, 1996
- [20] Keizer, J., *Statistical Thermodynamics of Nonequilibrium Processes*, Springer-Verlag, New York, 1987
- [21] Mayer, W. and Tamura, H., Propellant injection in a liquid oxygen/gaseous hydrogen rocket engine, *Journal of Propulsion and Power*, 12(6), 1137-1147, 1996
- [22] Miller, R. S., Harstad, K. and J. Bellan, J., Direct numerical simulations of supercritical fluid mixing layers applied to heptane nitrogen, in press, *J. Fluid Mech.*, 2001
- [23] Nomura, H., Ujiie, Y., Rath, H. J., Sato, J. and Kono, M., Experimental study on high pressure droplet evaporation using microgravity conditions, *Proc. of the Comb. Institute*, 26, 1267-1273, 1996
- [24] Oefelein, J. C. and Yang, V., Analysis of transcritical spray phenomena in turbulent mixing layers, AIAA 96-0085, 34th Aerospace Sciences Meeting, Reno, NV., 1996
- [25] Oefelein, J. C. and Yang, V., Analysis of hydrogen-oxygen mixing and combustion processes at high-pressures, AIAA 97-0798, 35th Aerospace Sciences Meeting, Reno, NV., 1997
- [26] Okong'o, N. and Bellan, J., Entropy production of emerging turbulent scales in a temporal supercritical n-heptane/nitrogen three-dimensional mixing layer, *Proc. of the Comb. Institute*, 28, 497-504, 2000
- [27] Okong'o, N. and Bellan, J., Direct numerical simulation of a transitional supercritical mixing layer: heptane and nitrogen, submitted to *J. Fluid Mech.*, 2000
- [28] Okong'o, N., Bellan, J. and Harstad, K., Consistent boundary conditions for multicomponent real gas mixtures based on characteristic waves, submitted to *J. Comp. Phys*, 2000
- [29] Okong'o, N. and Bellan, J., Linear stability analysis of real gas two- and three-dimensional mixing layers, submitted to *Phys. Fluids*, 2001
- [30] Sarman, S. and Evans, D. J., Heat flux and mass diffusion in binary Lennard-Jones mixtures, *Phys. Rev. A* 45(4), 2370-2379, 1992

- [31] Shuen, J-S., Yang, V. and Hsiao, G. C., Combustion of liquid-fuel droplets in supercritical conditions, *Combust. Flame*, 89, 299-319, 1992
- [32] Shuen, J-S. and Yang, V., Combustion of liquid-fuel droplets in supercritical conditions, AIAA 91-0078, 29th Aerospace Sciences Meeting, January 7-10, Reno, NV, 1991
- [33] Umemura, A., Supercritical liquid fuel combustion, *Proc. of the Comb. Institute*, 21, 463-471, 1986
- [34] Umemura, A. and Shimada, Y., Characteristics of supercritical droplet gasification, *Proc. of the Comb. Institute*, 26, 1621-1628, 1996
- [35] Yang, V., Lin, N. and Shuen, J-S., Vaporization of liquid oxygen (LOX) droplets in supercritical hydrogen environments, *Combust. Sci. and Tech.*, 97, 247-270, 1994

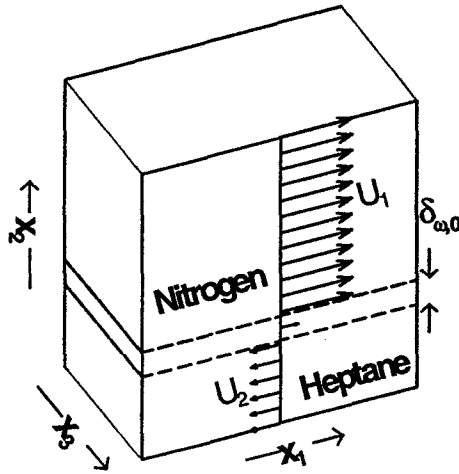


Figure 1: Shear layer configuration

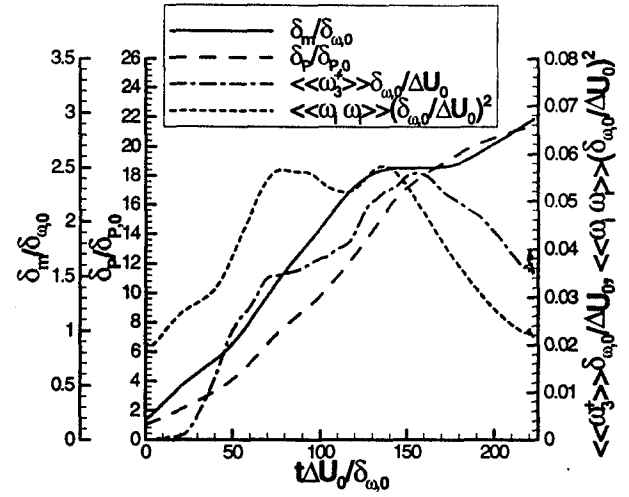


Figure 2: Global growth characteristics

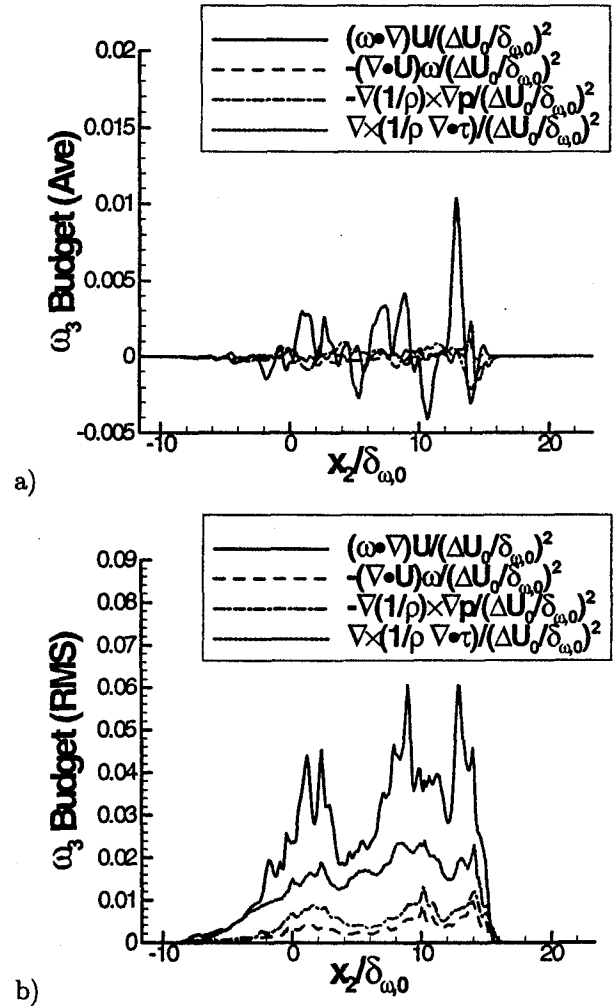


Figure 3: Spanwise vorticity budget at  $t^*=155$ , a) plane average and b) plane RMS.

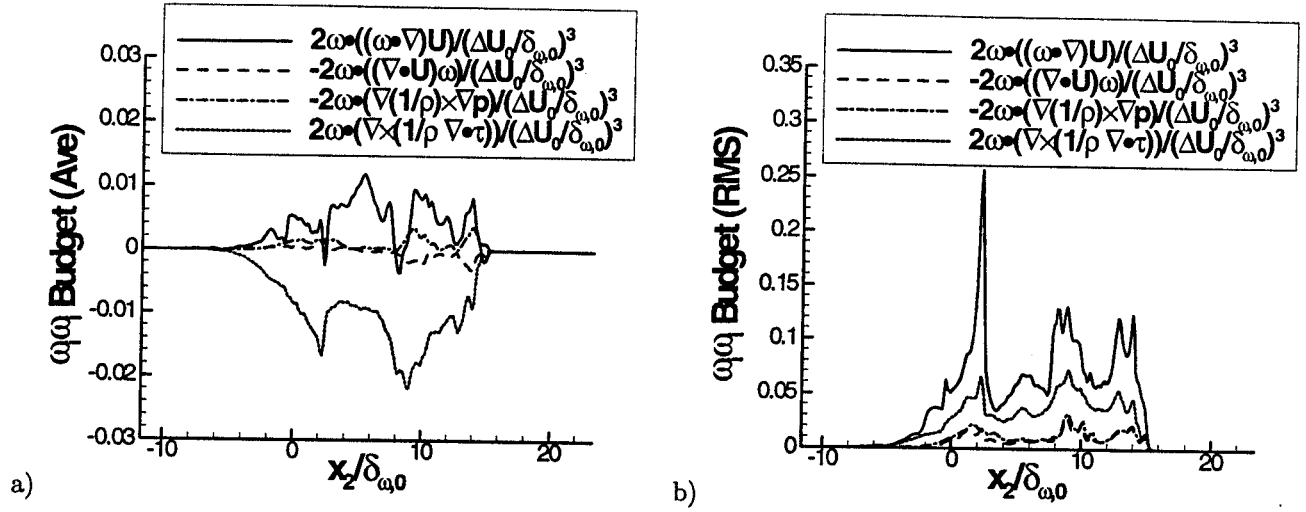


Figure 4: Vorticity magnitude budget at  $t^*=155$ , a) plane average and b) plane RMS.

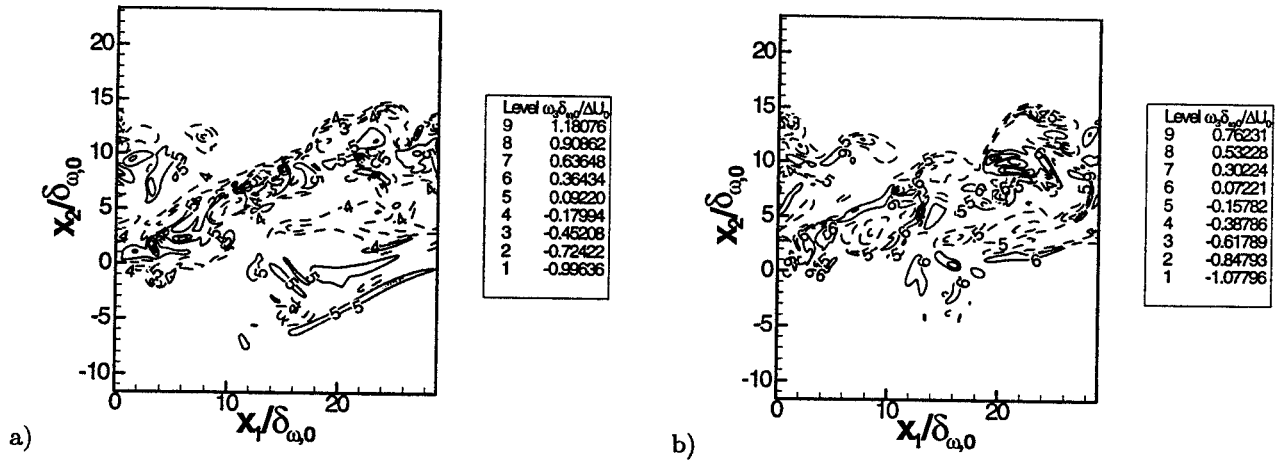


Figure 5: Spanwise vorticity at  $t^*=155$ , a) in the braid plane and b) in the between-the braid plane. (Negative vorticity contours are plotted with dashed lines.)

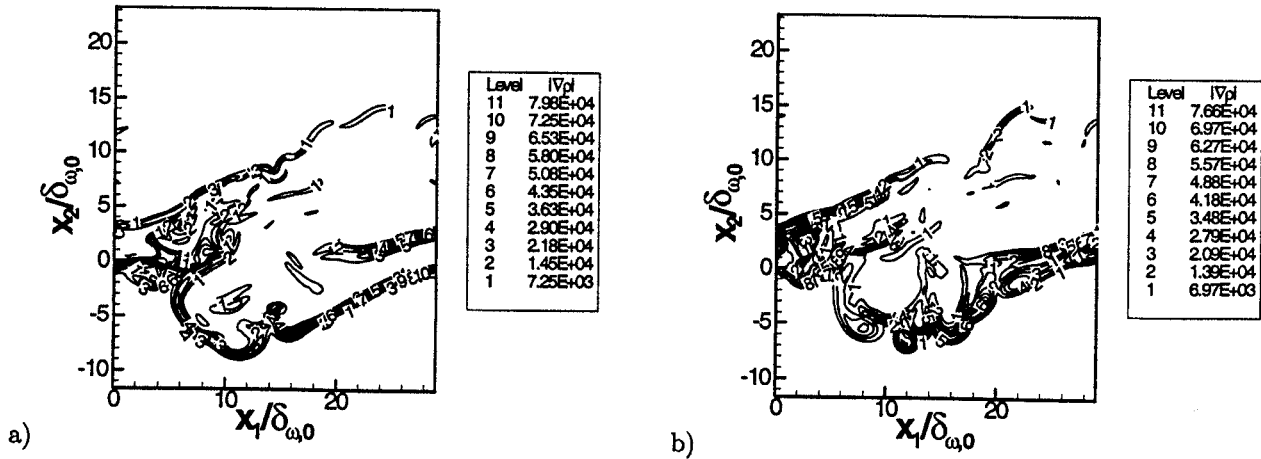


Figure 6: Density gradient magnitude at  $t^*=155$ , a) in the braid plane and b) in the between-the braid plane.



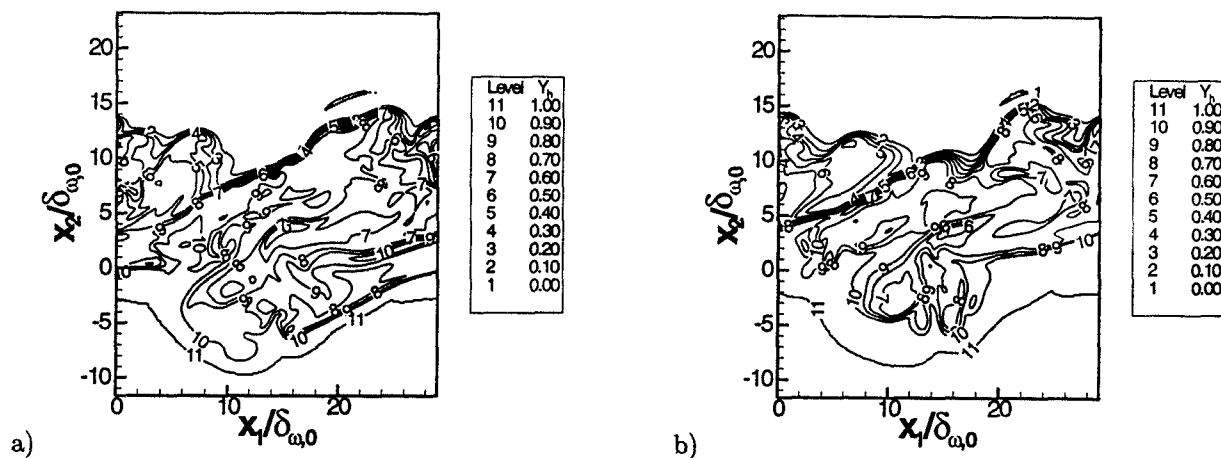


Figure 7: Heptane mass fraction at  $t^*=155$ , a) in the braid plane and b) in the between-the braid plane.

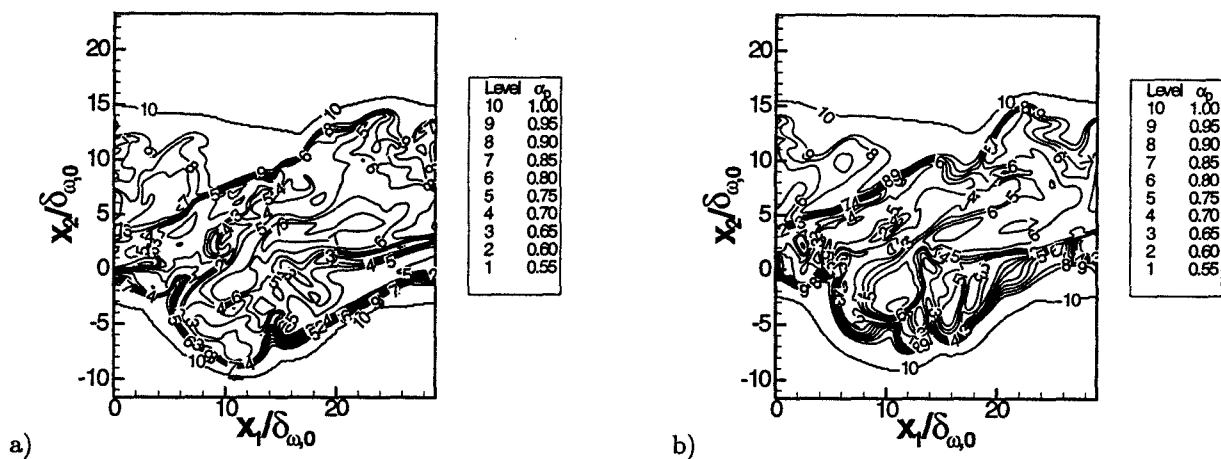


Figure 8: Mass diffusion factor at  $t^*=155$ , a) in the braid plane and b) in the between-the braid plane.

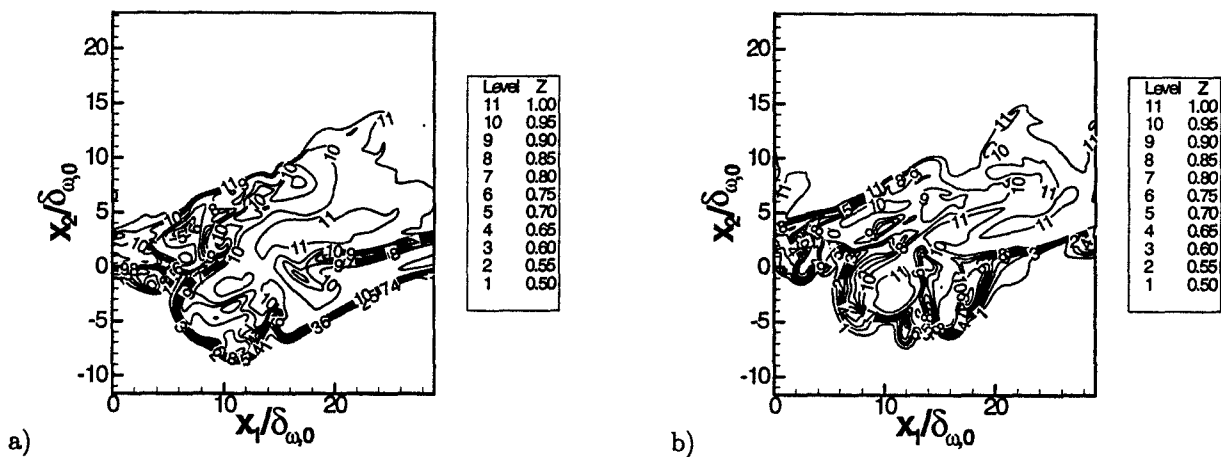


Figure 9: Compression factor at  $t^*=155$ , a) in the braid plane and b) in the between-the braid plane.